A. Yu. Danyk*, O. O. Sudakov

*Medical Radiophysics Department, Faculty of Radiophysics, Electronics and Computer Systems,
National Taras Shevchenko University of Kyiv, Kyiv, Ukraine*

*Corresponding author: antondanik@gmail.com

PHYSICAL BASES FOR DETERMINATION OF SCATTERING KERNELS FROM INCOMPLETE DATA IN GRID-LESS X-RAY IMAGING

A mathematical model for the determination of X-ray scattering kernels' shapes based on incomplete simulation or measurement data was introduced and tested using a mathematical phantom. The model is originally intended for low-dose X-ray imaging without anti-scatter grids. The proposed model fits different kinds of symmetrical and asymmetrical scattering kernels in different tissues well enough for practical applications. Kernels asymmetry is mostly caused by irradiation of the object near the boundaries of different tissues. The model describes a variety of asymmetrical kernels by proposed "sectoral" members. Application of the proposed model in scattering compensation procedure reduces resulting error up to 50 % for "wide" scattering kernels.

Keywords: X-ray image, scattered X-ray radiation convolution kernels, clustering analysis, segmentation, Monte-Carlo simulation, approximation, incomplete data.

1. Introduction

X-ray diagnostics in medicine relies on the analysis of projection images obtained by passing of X-rays through the living objects. X-ray radiation passed through the object is partially absorbed and scattered forming a shadow projection (Fig. 1).
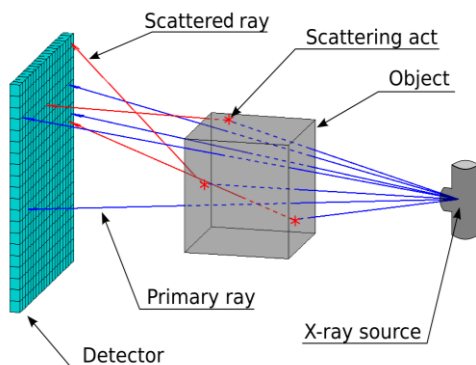

Fig. 1. X-ray imaging scheme.

The primary X-rays that were not absorbed or scattered form a sharp projection of the studied object's internal structure. The scattered rays form a fuzzy and slowly changing pattern in space – a background that distorts the desired image [1]. There is a number of hardware techniques that reduce the effect of scattered radiation on the quality of the resulting X-ray image by directly reducing the amount of scattered radiation falling on the detector. Such techniques (like anti-scatter grids) increase patients' dose because they also decrease primary radiation and expose increase is required [1]. There are also a number of methods allowing to correct the image obtained without using any hardware techniques and

without patient dose increase [2 - 5]. In [6 - 8] authors proposed a method for correcting X-ray images by means of "intellectual" deconvolution as follows:

1. A wide beam of X-ray tube radiation is represented as the sum of thin "pencil" beams. The radiation that is registered by the detector of the X-ray scanner is represented as a superposition of the primary and scattered radiation obtained during irradiation of the object with all of the mentioned thin beams.

2. The image of scattered radiation obtained during irradiation of the object with a pencil beam normalized by the intensity of recorded primary radiation is a local characteristic of the object – the scattering kernel (Fig. 2).

3. The resulting radiation M, recorded by the detector can be described by a simple expression (1). It implies that the object can be divided into a finite number of regions relatively homogeneous with respect to scattering. In the plane of the resulting X-ray image each such region is characterized by the scattering kernel K_i, measured image M_i, and primary image P_i:

$$M(x, y) = \sum_i M_i(x, y) =$$
$$= \sum_i P_i(x, y) + \sum_i \{P_i \cdot K_i\}(x, y). \qquad (1)$$

4. The primary radiation P can be recovered from the measured total radiation M by splitting the image into quasi-homogeneous regions and selecting a scattering kernel K_i for each region. The iterative recovery procedure can be represented in the form of expression

$$P_i = \Phi^{-1}\{\Phi\{M_i\}/[1+\Phi\{K_i\}]\},$$

$$S_i = \Phi^{-1}\{\Phi\{P_i\}\Phi\{K_i\}]\}, \quad M_i = P_i + S_i, \qquad (2)$$

where Φ and Φ^{-1} are forward and backward Fourier transforms, S_i – estimated scattering radiation image. The iterative procedure that involves intermediate estimation of scattering images S_i is one of the most stable approaches.

Initial segmentation of the image into regions M_i and assignment of appropriate kernels K_i is performed by a specially trained support vector machine classifier that takes into account image pixels' statistical properties [6 - 8]. The tasks of kernels accumulation and image segmentation for kernels selection were studied in [6 - 8]. Errors in kernels' shape significantly influence the estimated primary radiation image, especially for "wide" scattering kernels.
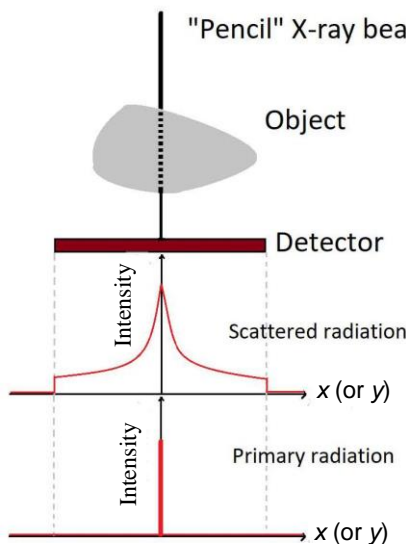
The scattering kernel is essentially the X-ray image obtained by irradiating the object with a pencil beam. It means that the kernel can be only determined in the spatial region covered by the detector. It is easy to notice that image correction requires the scattering kernels to be known in a spatial region with a size at least twice the size of the corrected image (e.g., correction at the image boundary requires the kernel to be known at another image boundary and vise verse) (Figs. 2 and 3). In most practical cases detector size corresponds to the investigated object size and scattering kernels' data outside the detector are unknown. Thus, measured, or simulated data for scattering kernels are incomplete and kernels extrapolation is required.
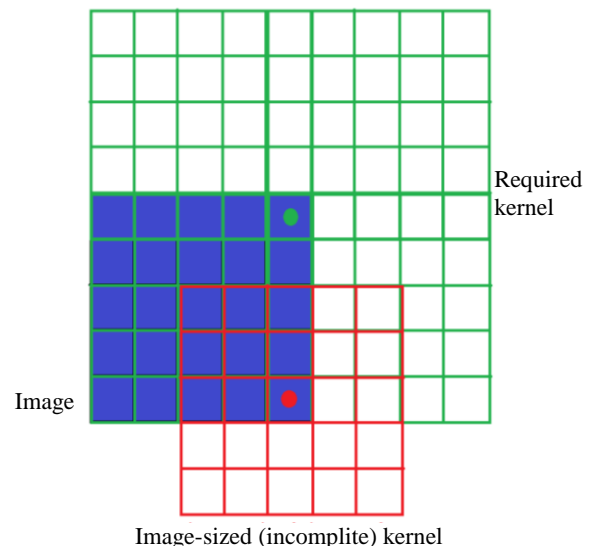

Fig. 2. X-ray pencil beam: scattering kernel genesis.

Fig. 3. Kernel size problem.

Scattering kernels parametrization or approximation using a simple function is required not only for kernels extrapolation in the scenario mentioned above but also as a more efficient interpolation method for "beam-stop" schemes [9], to scale the scattering kernels for different object sizes, for prediction of kernels for the new object, etc.

There are a number of works devoted to kernels parametrization. Gaussian-like scattering kernels were introduced in [3, 10]. Such kernels are good for calculations but significantly differ from real kernels and introduce errors.

In the present work, we suggest a simple kernel approximation based on the physics of X-ray scattering that can fit symmetrical as well as asymmetrical kernels for a large variety of tissues.

2. Scattered radiation

Accurate estimations of scattering kernels for any object may be performed only by Monte-Carlo simu-

lations with a large number of empirical tissues' parameters. Scattered radiation also could be estimated using analytical approaches, but the accuracy of such estimations is low. Analytical methods apply only to simple homogenous or heterogeneous smooth geometry objects. Even in such cases, the problem remains too complex to find the exact solution. In most works, only the Compton process is accounted for neglecting the Rayleigh scattering as well as multiple scattering processes. One of the simplest scattered radiation estimations is made for the model presented in Fig. 4 of [11]. The object is assumed to be an infinite plate of constant thickness t located on the distance g from the detector and irradiated by a mono-energetic "pencil" beam (beam with a very small width that can be described by Dirac delta function) that falls normally to the surface of the object.
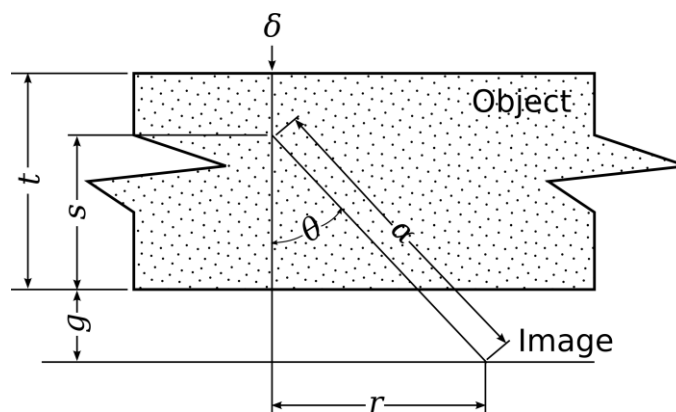
Fig. 4. Simple homogeneous model.

After applying the simplified Klein - Nishina formula for Compton scattering differential cross-section and Berr - Lambert law for primary radiation

$$I_S(r) = K \int_{s=0}^{t} \exp[-(t-s)] \exp(-\mu_S \alpha)(2\sin\theta - \sin^3\theta)\left(\frac{1}{s+g}\right)\left[1 + \left(\frac{r}{s+g}\right)^2\right] ds, \quad (3)$$

where $\theta = tan^{-1}[r/(s+g)]$; $\alpha = [s/(s+g)][r^2 + (s+g)^2]^{1/2}$; μ_p, μ_s – effective linear attenuation coefficients of the primary beam and scattered radiation respectively; K is the experimental constant dependent on the object thickness, beam energy, and objects' material. This constant eliminates the dependence on the X-ray source intensity by normalization of this source intensity such as the total area of integral I_S becoming equal to the scatter-to-primary ratio $SPR = \int_{-\infty}^{\infty} I_S(r) dr$ for given object thickness and source spectrum. The value of SPR can be experimentally measured or numerically estimated [12].

The analytical model is closely correlated to Monte-Carlo simulation results with respect to the mentioned constant K [9].

Significant improvements in this scheme were proposed in [13]. Authors introduce up to two materials (heterogeneous model) with more complicated but still smooth geometry (tested on the slabs and cylinder) and poly-energetic spectrum of the X-ray source.

Using Monte-Carlo simulation of X-ray interaction with simple phantoms, like slabs, cylinders with one layer of material (homogeneous case), or two layers of material (heterogeneous case) authors proved that this model predicts the shape of the scattered radiation distribution with high accuracy (from 2 % error for the mono-energetic case and up to 8 % error in poly-energetic case).

Analytical models are useful for homogeneous objects with simple geometry (e.g., mammography) but become too complex otherwise.

attenuation the scattered radiation estimator looks like the expression

Scattering kernels parametrization

A decent approximation for scattered X-ray radiation distributions with few parameters maybe obtained from solutions of X-ray radiative transport equation [14, 15]

$$\vec{n}\vec{\nabla}_r L(\vec{r},\vec{n},\lambda) + \left(\mu_s(\vec{r},\lambda) + \mu_a(\vec{r},\lambda)\right) L(\vec{r},\vec{n},\lambda) =$$

$$= \mu_s(\vec{r},\lambda) \int_{\Omega,\Lambda} L(\vec{r},\vec{n},\lambda) w(\vec{r},\vec{n},\vec{n}',\lambda,\lambda') d\vec{n}' d\lambda' + L_p(\vec{r},\vec{n},\lambda), \quad (4)$$

where $L(\vec{r},\vec{n},\lambda)$, $L_p(\vec{r},\vec{n},\lambda)$ – radiance (intensity) of total and primary X-rays with wavelength λ passing point $\vec{r}$ at direction $\vec{n}$; $\mu_s(\vec{r},\lambda)$ and $\mu_a(\vec{r},\lambda)$ distributions of scattering and absorption coefficients; $w(\vec{r},\vec{n},\vec{n}',\lambda,\lambda')$ – angular distribution (indicatrix) of scattering that is inelastic in general (scattered wavelength is changing from λ' to λ); $\vec{\nabla}_r$ – spatial gradient.

For totally isotropic medium and independence of scattering from wavelength, the scattered radiation from (4) satisfies diffuse approximation [14]

$$-\vec{\nabla}_r A(\vec{r}) \vec{\nabla}_r I_s(\vec{r}) + B(\vec{r}) I_s(\vec{r}) = I_p(\vec{r}), \quad (5)$$

where A and B – coefficients that depend on μ_s and μ_a; $I_s(\vec{r}) = \int L_s(\vec{r},\vec{n},\lambda) d\vec{n} d\lambda$ and $I_p(\vec{r}) = \int L_p(\vec{r},\vec{n},\lambda) d\vec{n} d\lambda$ – spatial density of scattered and primary radiation energy.

For spatial uniform medium the fundamental solution of (5) has a form

$$I_0(r) = \frac{\alpha e^{-\beta r}}{r} = \alpha e^{-\log(r) - \beta r} \qquad (6)$$

where α and β are constants dependent on absorption and scattering coefficients, r – spherical coordinates system radius. Equation (6) gives scattering kernel for uniform and isotropic medium, monochromatic radiation, and elastic scattering. Realistic cases will introduce perturbations into (6).

According to Monte-Carlo simulations [7] scattering kernel is a function with a significant cylindrical symmetry. It has a sharp peak at its center because forward scattering is a significant part of scattered photons. Kernel rapidly decreases to the periphery. The more symmetrical and homogenous objects have the more symmetrical scattering kernel.

Taking these facts into account we suggest approximating the scattering kernels in the form (7) that is constructed taking Eq. (6) into account:

$$I_s(\theta, r) = A_0 + A_1 \cdot \exp\left\{ \frac{C_{01}\sqrt{r} + \sum_{j=2}^{N_r} C_{0j}r^j}{\left(1 + \sum_{i=1}^{N_\theta}|B_i|\right)} + \frac{\sum_{i=1}^{N_\theta}\left(B_i \cdot e^{-\left(\frac{|\theta - \bar\theta_i|}{\sqrt{2}\sigma_i}\right)^m} \cdot \left[C_{i1}\sqrt{r} + \sum_{j=2}^{N_r} C_{ij}r^j\right]\right)}{\left(1 + \sum_{i=1}^{N_\theta}|B_i|\right)} \right\}, \qquad (7)$$

where, θ, r – polar coordinates in image plane; A, B, C, θ, σ – are the free model parameters; N_r – parameter that defines the r polynomial order (starting from $r^{0.5}$); N_θ – parameter that defines an amount of "extra" sectors in the kernel; m – define the shape of the Gaussian windows for each "extra" sector. The kernel is applied to the image pixel with coordinates x_c, y_c.

There is a simple idea that stands behind the expression above:

scattering kernel rapidly falls on distance (r) – that's why there is an exponent from an r polynomial (extension of (3) and (6));

the polynomial under the exponent could have different order - due to undefined object's geometry and homogeneity;

the resulting scattering kernel is expected to have a specific angular asymmetry, especially in the case of an object with several "quasi-homogeneous" regions and a border that separates these regions near the point the scattering kernel is estimated for. Some sectors (or angular parts) could be amplified, attenuated, or just have another dumping law – that's why the "extra" sector modifier (the second part of an expression inside of { } brackets in (7)) was added;

Gaussian window defined by parameter m was added just to shape a "sector" transition.

3. Numerical simulation

The proposed model was tested on the scattering kernels obtained for the mathematical phantom described below during the scattering compensation procedure proposed in [7]. Scattering kernels were accumulated during the training simulation and the testing X-ray images – the testing simulation.

Mathematical phantom

Training and testing simulations were performed using the same phantom given in Fig. 5. It consists of two cylinders (filled with calcium (1) and with air (2)) placed in the water box (3). The water box's size is $400 \times 400 \times 100$ mm. Calcium cylinder thickness is 5 mm and air cylinder is 40 mm. Both cylinders have the same diameter of 120 mm and are located equidistantly along the x-axis at 100 mm from the center.
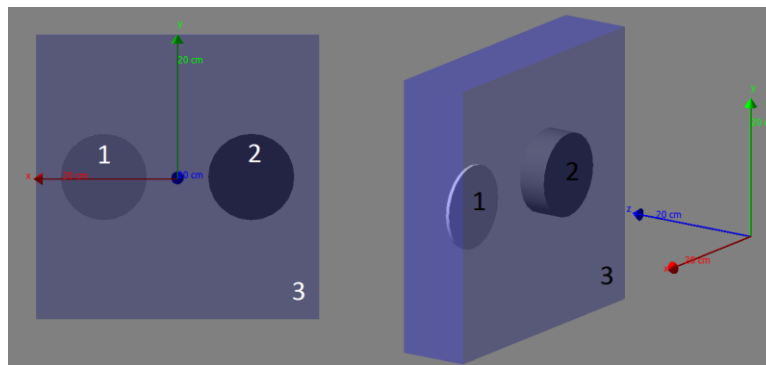

Fig. 5. Mathematical phantom.

Training and testing simulations

Interactions of X-rays with the phantom were simulated using the Monte-Carlo method (training and testing simulations made by the GATE [16] software package).
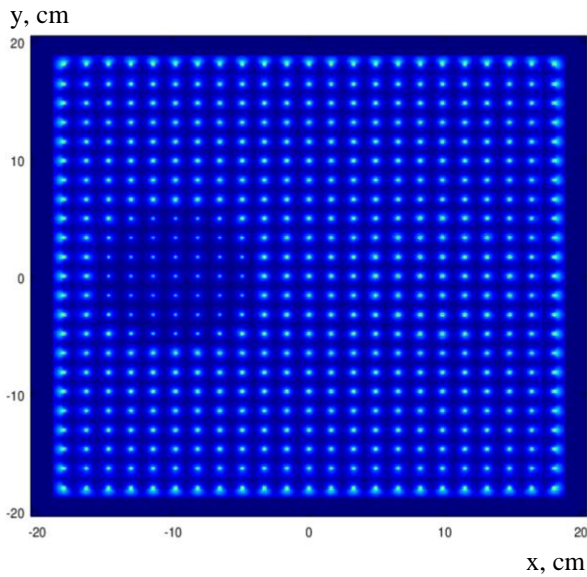
y, cm

Fig. 6. Scattering kernels map.

To provide a training simulation, the phantom was divided into 625 square regions that correspond to the resolution of 1.704 cm. The detector was twice bigger than a phantom with the same 1.3 cm resolution (49×49 pixels). Each area was irradiated with a pencil beam of a realistic X-ray tube energy spectrum with a maximum of 75 keV. Physical pro-

cesses, such as photoelectric effect, Compton scattering, Rayleigh scattering, and synchrotron radiation, were considered. The full set of 625 scattering kernels were obtained (Fig. 6). Air cylinder offers significantly less absorption and scattering than calcium cylinder and water. Thus, air cylinder passes more primary radiation that further scatters in water resulting in slightly brighter kernels' images. Calcium cylinder significantly absorbs primary radiation and less radiation further scatters in water providing significantly darker kernels' images. Borders with air offer very few scatterings resulting in very dark kernels' images.

Testing simulation differs from the training one by a smaller detector (object-sized detector with the same resolution – 25×25 pixels) and different X-ray irradiation scenario – wide straight beam irradiated the whole object instead of a pencil beam that irradiates the object locally.

Scattering kernels parametrization evaluation

Three different kernel types were selected for this object: symmetrical small and very sharp kernels obtained while irradiating an air outside the water box (*a*); quite symmetrical and less sharp than the first scattering kernel (*b*); asymmetrical and wide kernels obtained mostly on different edges (object-to-air edge, cylinders-to-water box edges) (*c*). These scattering kernels were fitted to the proposed model (7) using $m = 8$ and different values for $N_r = 0, ..., 5$ and $N_\theta = 0.1$ (Fig. 7).
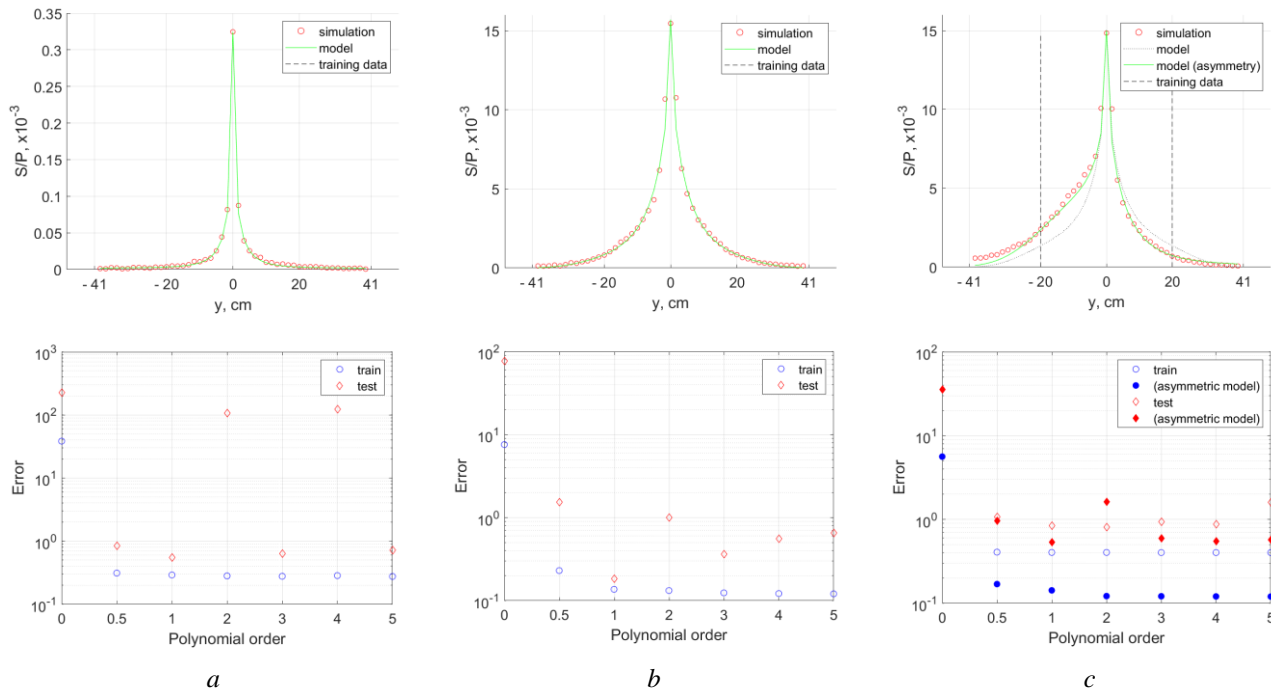

Fig. 7. Scattering kernels: fitting to the model (top part shows central slices scattering kernels).

The model was fitted using the central part of the scattering kernels (known as central 25×25 points).

Fig. 7 shows the result of scattering kernels (*a*) and (*b*) fitted with $N_\theta = 0$ (symmetrical model) and the kernel (*c*) – with $N_\theta = 0.1$ (model with and without sectoral asymmetry). Most kernels may be approximated using the model of orders up to 1. Few kernels require N_r up to 3 and this order was chosen. Scattering kernel (*c*) fitting is also shown in Fig. 8.
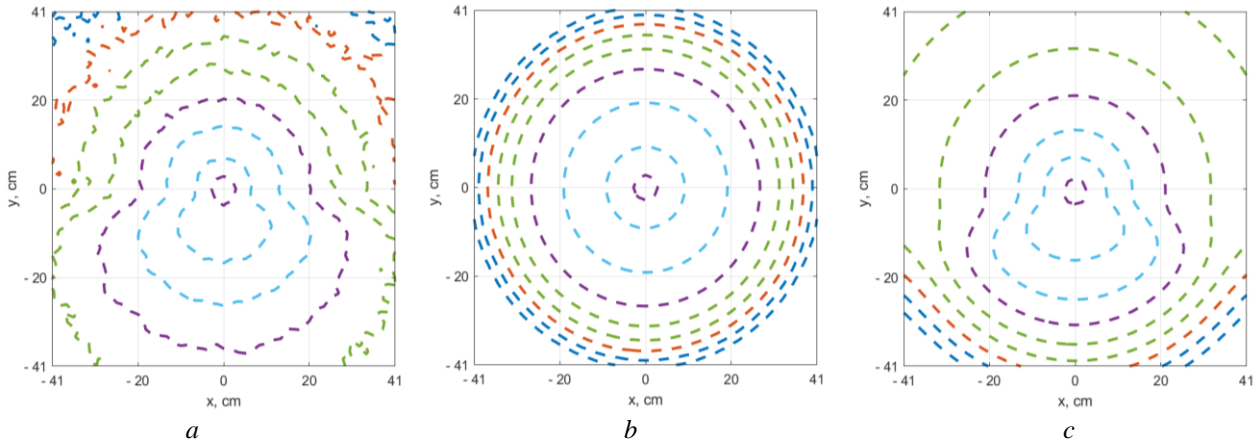

Fig. 8. Asymmetric kernel: measured values (*a*), symmetrical model (*b*), asymmetrical model (*c*).

The top part of the figure shows the scattering kernel's shape along with the fitted model for $N_r = 3$. The bottom part of the figure shows an error dependent on the polynomial order used estimated by the expression

$$Error = \frac{\sqrt{\sum \left(K_{fitted} - K \right)^2 / size(K)}}{\sum K / size(K)}, \qquad (8)$$

where K and K_{fitted} are values of scattering kernels and fitted model in the central part (25×25 points) for training error and outside the central part for testing error, $size(K)$ – number of pixels in the kernel image.

Increasing the N_θ does not improve the error and that's why $N_\theta = 1$ and $N_r = 3$ were chosen as optimal values for obtained scattering kernels library.

Finally, the following four scattering kernels (from different scattering kernels libraries) were tested during the scattering optimization procedure: "wide" kernels – originally known values for measured kernels; "narrow" kernels – the central part of the original values for measured kernels with zeros outside (incomplete kernel); "fully approximated" kernels - values of the model fitted to the "narrow" kernels; "approximated corners" kernels – "narrow" kernels values inside the central part with "fully approximated" kernels values outside.

4. Results and discussion

The testing simulation was made for several exposure times. Scattering compensation was performed for scattering kernels libraries shrunk to the different number of scattering kernels by clustering analysis [6, 7]. Scattering compensation quality was estimated using error definition (9). Differential error is a maximum value of (9) in the image, and integral error is the average value of the expression

$$Error = \left| \frac{P_{recovered} - P_{original}}{P_{original}} \right|. \qquad (9)$$

The errors were estimated for the different scenarios as follows. The error as a function of scattering kernels library size for the largest exposure time is shown in Fig. 9. The error as a function of exposure time for fixed scattering kernels library size (10 clusters) is given in Fig. 10.
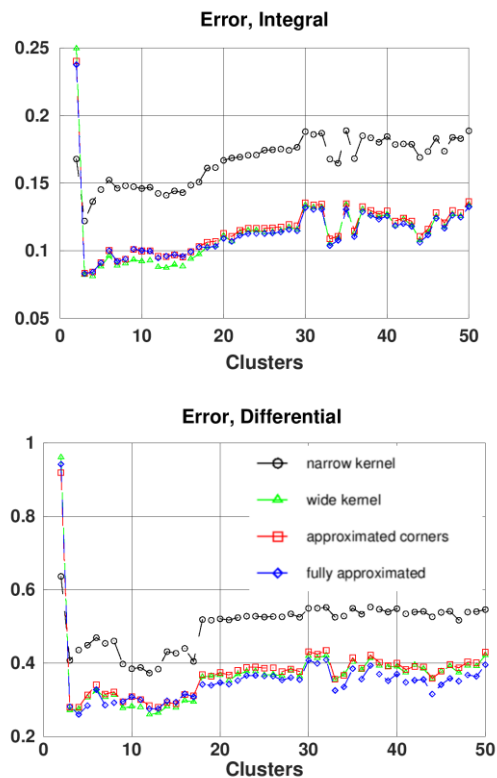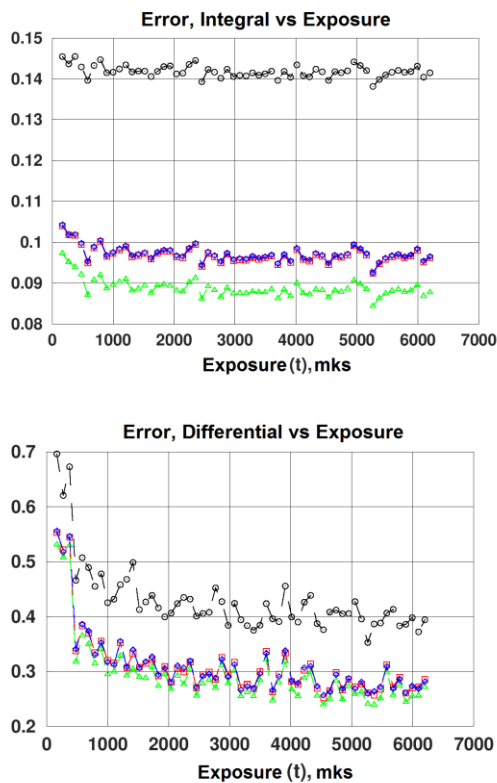

Fig. 9. Error vs Library size.

Fig. 10. Error vs Exposure.

Some scattering kernels corners (values outside the known central part of the kernel) contain up to 30 % extra energy in comparison to the central known part. That is why the application of wider scattering kernels ("wide", "approximated corners", and "fully approximated" kernels) provide lower error compared to incomplete kernels. The proposed scattering kernel model performs well according to

Figs. 9 and 10. Error-values for the original "wide" kernels application are very close to the "model" kernels cases (with just a little better result for the first one). For some very small and very large amounts of kernels, the approximation provides a slightly smaller error than wide kernels. Approximated kernels are smoother than computed with the Monte-Carlo method and can provide a more stable approximation of scattered radiation image that is smooth by nature.

5. Conclusions

The proposed model tested on a simple phantom demonstrated good results in the fitting of different scattering kernel types. Kernels asymmetry is mostly caused by irradiation of the object near the boundaries of different tissues. The model fits the asymmetrical kernels by virtue of "sectoral" member presence. The scattering compensation procedure provides up to 50 % less error in the case of extrapolated kernels application compared to incomplete kernels. Almost ideal fitting results were achieved for the simple phantom. The largest errors are obtained at the boundaries of asymmetric kernels. Application of the model to real objects is expected to provide not so good results but these results are expected to be much better than for the application of kernels with incomplete outside data.

REFERENCES

1. M.A. Flower (ed.). *Webb's Physics of Medical Imaging*. 2-nd ed. (CRC Press, 2012) 812 p.
2. A. Danyk. The problem of scattered radiation in X-ray imaging. Bulletin of Taras Shevchenko National University of Kyiv. Ser.: Physics and Mathematics 1 (2018) 72.
3. Z. Wei et al. A patient-specific scatter artifacts correction method. In: Proc. SPIE 9033. Medical Imaging 2014: Physics of Medical Imaging, San Diego, California, United States, 19 March 2014.
4. K. Kim et al. Fully iterative scatter corrected digital breast tomosynthesis using GPU-based fast Monte Carlo simulation and composition ratio update. Medical Physics 42 (2015) 5342.
5. J. Maier et al. Deep scatter estimation (DSE): feasibility of using a deep convolutional neural network for real-time x-ray scatter prediction in cone-beam CT. In: Proc. SPIE 10573. Medical Imaging 2018: Physics of Medical Imaging, Houston, Texas, United States, March 9, 2018.
6. A. Danyk, S. Radchenko, O. Sudakov. Optimization of Grid-less Scattering Compensation in X-ray Imaging: Simulation Study. In: Proc. of the 37-th IEEE Intern. Conf. on Electronics and Nanotechnology (ELNANO), Kyiv, Ukraine, April 18 - 20, 2017. P. 316.
7. A. Danyk et al. Using clustering analysis for determination of scattering kernels in X-ray imaging. In: Proc. of the 10-th IEEE Intern. Conf. on Intelligent Data Acquisition and Advanced Computing Systems: Technology and Applications, IDAACS, Metz, France, September 18 - 21, 2019. P. 211.
8. A. Danyk, O. Sudakov. Optimized Estimation of Scattered Radiation for X-ray Images Improvement: Realistic Simulation. Radioelectronics and Communications Systems 63 (2020) 387.
9. J.P. Shah, S.D. Mann, M.P. Tornai. Characterization of X-ray scattering for various phantoms and clinical breast geometries using breast CT on a dedicated hybrid system. Journal of X-ray Science and Technology 25 (2017) 373.
10. J.L. Ducote, S. Molloi. Scatter correction in digital mammography based on image deconvolution. Physics in Medicine & Biology 55 (2010) 1295.

11. J.M. Boone, J.A. Seibert. An analytical model of the scattered radiation distribution in diagnostic radiology. Medical Physics 15 (1988) 721.

12. M. Honda, K. Kikuchi, K. Komatsu. Method for estimating the intensity of scattered radiation using a scatter generation model. Medical Physics 18 (1991) 219.

13. W. Yao, K.W. Leszczynski. An analytical approach to estimating the first order x-ray scatter in the heterogenous medium. Medical Physics 36 (2009) 3145.

14. A. Liemert, A. Kienle. Exact and efficient solution of the radiative transport equation for the semi-infinite medium. Scientific Reports 3 (2013) 1.

15. D.M. Paganin, S.M. Kaye. X-ray Fokker-Planck equation for paraxial imaging. Scientific Reports 9 (2019) 1.

16. D. Sarrut et al. A review of the use and potential of the GATE Monte Carlo code for radiation therapy and dosimetry applications. Medical Physics 41(6) (2014) 064301.

17. O. Sudakov et al. User Clients for Working with Medical Images in Ukrainian Grid Infrastructure. In: Proc. of the 7-th IEEE Intern. Conf., IDAACS, Berlin, Germany, September 12 - 14, 2013. P. 705.

А. Ю. Даник*, О. О. Судаков

*Кафедра медичної радіофізики, факультет радіофізики, електроніки та комп'ютерних систем
Київського національного університету імені Тараса Шевченка, Київ, Україна*

Відповідальний автор: antondanik@gmail.com

ФІЗИЧНІ ОСНОВИ ВИЗНАЧЕННЯ ФУНКЦІЙ ЯДРА РОЗСІЮВАННЯ ЗА НЕПОВНИМ НАБОРОМ ДАНИХ У БЕЗРАСТРОВІЙ РЕНТГЕНОГРАФІЇ

Запропоновано та випробувано за допомогою математичного фантома математичну модель форми ядер розсіювання рентгенівських променів на основі неповних даних моделювання. Передбачено використання моделі для потреб низькодозової рентгеноскопії без застосування протирозсіювальних растрів. Запропонована модель підходить для різних типів симетричних та асиметричних ядер розсіювання різних тканин у достатній для практичного використання мірі. Асиметрія ядер здебільшого виникає при опроміненні меж поділу різних тканин. Модель описує широке коло асиметричних ядер завдяки запропонованому «секторному» доданку. Використання запропонованої моделі при компенсації розсіяного випромінювання зменшує результуючу похибку компенсації до 50 % у порівнянні з результатами використання вузьких ядер.

Ключові слова: рентгенівське зображення, згорткові ядра розсіяного рентгенівського випромінювання, кластерний аналіз, сегментація, симуляція методом Монте-Карло, апроксимація, неповні дані.